Scale-Up Tests of High Regression Rate Paraffin-Based Hybrid Rocket Fuels

Arif Karabeyoglu[*]
Stanford University, Stanford, California 94305
Greg Zilliac[†]
NASA Ames Research Center, Moffet Field, California 94035
Brian J. Cantwell[‡]
Stanford University, Stanford, California 94305
Shane DeZilwa[§]
NASA Ames Research Center, Moffet Field, California 94035
and
Paul Castellucci[¶]
Stanford University, Stanford, California 94305

Recent research at Stanford University has led to the identification of a class of paraffin-based fuels that burn at surface regression rates that are three to four times that of conventional hybrid fuels. The approach involves the use of materials that form a thin, hydrodynamically unstable liquid layer on the melting surface of the fuel. Entrainment of droplets from the liquid–gas interface substantially increases the rate of fuel mass transfer, leading to much higher surface regression rates than can be achieved with conventional polymeric fuels. Thus, high regression rate is a natural attribute of the fuel material, and the use of oxidizing additives or other regression rate enhancement schemes is not required. The high regression rate hybrid removes the need for a complex multiport grain, and most applications up to large boosters can be designed with a single port configuration. The fuel contains no toxic or hazardous components and can be shipped by commercial freight as a nonhazardous commodity. At the present time, grains up to 0.19 m [19.1 cm (7.5 in.)] in diameter and 1.14 m [114.8 cm (45.2 in.)] long are fabricated in a general-purpose laboratory at Stanford University. To further demonstrate the feasibility of this approach, a series of scale-up tests with gaseous oxygen have been carried out using a new Hybrid Combustion Facility (HCF) at NASA Ames Research Center. Data from these tests are in agreement with the small-scale, low-pressure, and low mass flux laboratory tests at Stanford University and confirm the high regression rate behavior of the fuels at chamber pressures and mass fluxes representative of commercial applications.

Nomenclature

A_{or}, A_n	=	sonic orifice and nozzle throat areas
A_{port}	=	area of the fuel port
a	=	regression rate coefficient
B_G	=	flux equation coefficient
C_d, C_D	=	discharge coefficients of nozzle and sonic orifice
C_{port}	=	circumference of the fuel port
c^*_{act}, c^*_{theo}	=	measured and theoretical characteristic velocities
c^*_{ox}	=	characteristic velocity of ambient gaseous oxygen
D_{ratio}	=	d_{vc}/d_f
d_f, d_i	=	final and initial port diameters
d_{vc}	=	port diameter at valve closing
E	=	relative error
f_R, f_T	=	sensitivity coefficients
G	=	local mass flux
G_{ox}, G_{tot}	=	oxidizer and total mass fluxes
L_g	=	grain length
m	=	length exponent
$\dot{m}$	=	local mass flow rate
$\dot{m}_{ox}$	=	oxidizer mass flow rate
$\dot{m}_{ox}^{ter}$	=	oxidizer mass flow rate at valve closing event
n	=	flux exponent
P_c, P_f	=	chamber and feed system pressures
R	=	$\tau_{fs}\dot{r}^{ter}/d_f$
$\dot{r}$	=	fuel regression rate
$\dot{r}^{ter}$	=	fuel regression rate at valve closing event
T	=	nt_f/τ_{fs}
t_b	=	burn time
t_f	=	thrust termination time
V_f	=	feed system volume
x	=	axial distance
α	=	mass flux distribution coefficient
γ	=	ratio of the specific heats for oxygen at ambient temperature
ΔM_f	=	mass of burned fuel
ΔM_{ox}	=	mass of oxidizer burned
η_c	=	combustion efficiency
ρ_f	=	fuel density
τ_{fs}	=	characteristic time scale of the feed system
$-$	=	averaged quantity

[*]Senior Research Engineer, Department of Aeronautics and Astronautics. Member AIAA.
[†]Research Scientist. Member AIAA.
[‡]Professor, Department of Aeronautics and Astronautics. Fellow AIAA.
[§]National Research Council Postdoctoral Fellow. Member AIAA.
[¶]Graduate Student, Department of Aeronautics and Astronautics, Stanford University, Member AIAA.

Introduction

THE hybrid rocket has been known for over 50 years, but was not given serious attention until the 1960s. The primary motivation

was the nonexplosive character of the fuel, which led to safety in both operation and manufacture. The fuel could be fabricated at any conventional commercial site (even at the launch complex) with no danger of explosion. Thus, a large cost saving could be realized both in manufacture and launch operation. Compared to a solid rocket, the hybrid is much less sensitive to cracks and debonds in the propellant, has a higher specific impulse I_{sp}, and can be throttled including shutdown and restart on demand.[1–4]

The hybrid enjoys several advantages over a liquid system. One of the main advantages is a reduced explosion hazard because an intimate mixture of oxidizer and fuel is not possible. In addition, the hybrid rocket requires one rather than two liquid containment and delivery systems. The complexity is further reduced by omission of a regenerative cooling system for both the chamber and nozzle. A wide throttle range is relatively easy to achieve in a hybrid where throttling the oxidizer automatically throttles the fuel and there is no requirement to match the momenta of the dual propellant streams during the throttling operation. Throttling ratios up to 10:1 have been demonstrated in hybrid motors.

Last, the fact that the fuel is in the solid phase makes it very easy to add solid performance-enhancing materials such as aluminum. This enables the hybrid to gain a specific impulse I_{sp} and density advantage over a comparable hydrocarbon-fueled liquid system. Additionally, metal additives can be used to reduce the oxidizer-to-fuel (O/F) ratio for maximum specific impulse, thereby enabling a reduction in the required mass of liquid oxidizer.

The principal disadvantage of the conventional hybrid rocket is the inherent low burning rate caused by the diffusive nature of the combustion process. Hence, traditional hybrid motor designs have required multiport grain geometries to achieve the required thrust levels. However, recent research at Stanford University has led to the identification of a class of fast burning fuels that form a hydrodynamically unstable liquid layer over the their surface.[5–8] A theory that explains the behavior of liquefying fuels has been developed and has been used to identify fuel properties that will produce droplet entrainment.[7,8] A fast burning paraffin-based fuel has been formulated and tested in a laboratory-scale motor at Stanford University. Regression rates three to four times higher than that of conventional hybrid fuels, that is, hydroxyl-terminated polybutadiene (HTPB), have been observed.[6,7]

In this paper, we discuss the scale-up testing program on paraffin-based fuels and the results obtained from the 19.1 cm (7.5 in.) diam, that is, grain outside diameter, tests conducted at the Hybrid Combustion Facility (HCF) at the NASA Ames Research Center.

Ames Hybrid Combustion Facility

To further demonstrate the feasibility and scalability of paraffin-based fuels, a new hybrid combustion test facility has been developed at NASA Ames Research Center. The Ames Hybrid Combustion Facility consists of an oxygen delivery system, a methane/oxygen-based gas–gas ignition system, and a combustion chamber as shown schematically in Fig. 1. The oxygen feed system is capable of delivering up to 16 kg/s of ambient-temperature gaseous oxygen to the combustion chamber at combustion chamber pressures that range between approximately 10 atm (150 psi) and 68 atm (1000 psi). During operation of the facility, a proportional, integral, derivative-based feedback control system maintains a constant pressure upstream of the sonic orifice (by controlling the flow through a control valve) thereby establishing a constant oxygen mass flow rate that is decoupled from pressure fluctuations in the combustion chamber.

Combustion takes place in an insulated chamber that is roughly 120.1 cm (47.3 in.) long with an inside diameter of 19.49 cm (7.672 in.) and steel walls that are 3.18 cm (1.25 in.) thick. The fuel is contained in a paper phenolic cartridge that is inserted by removing threaded tie rods and sliding the combustion chamber components apart. During operation, gaseous oxygen (GOX) is fed to one end of the chamber and the exhaust exits through a convergent ATJ-grade graphite nozzle on the opposite end of the combustion chamber.

Standard measurements during a run of the facility include time histories of chamber pressure and oxygen mass flow rate. The cham-
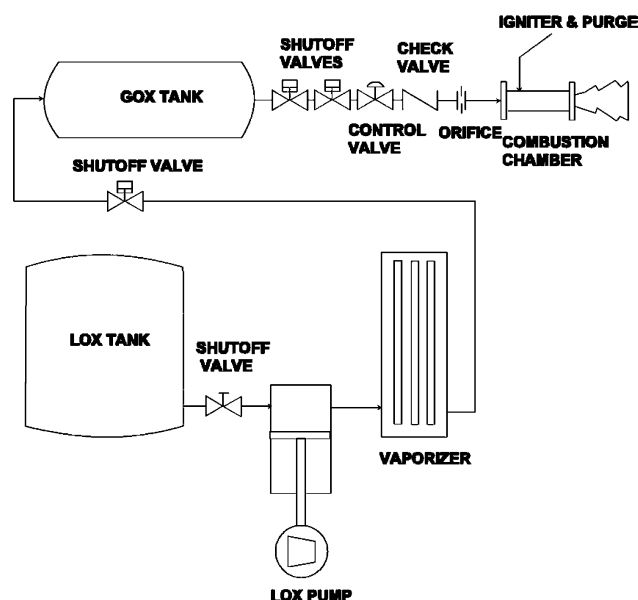

Fig. 1   Simplified schematic of the Ames Hybrid Combustion Facility.

ber pressure is measured at the fore-end of the motor using a Kistler 601B transducer to resolve the fast-varying component of the pressure and a Rosemount model 1151 pressure transducer for the dc component. Typical data sampling rate is 1000 Hz.

The facility became operational in September 2001, and since then, a series of tests have been undertaken on intermediate-scale motors at pressures and mass fluxes representative of commercial applications.

Grain Fabrication

Fuel grains are produced using a centrifugal casting process designed to produce crack-free and void-free grains. Paper phenolic tubes are used as the fuel cartridge. An annular, ATJ-grade graphite insulator is bonded inside each end of tube, using a high-temperature epoxy. These insulators have a dual purpose. When casting fuel grains, the graphite insulators mate with Teflon®-coated, polyethylene plugs that seal in the contents of the phenolic tube. When testing, the ATJ-grade graphite components mate with pre- and post-combustion chamber insulators to prevent the external flow of combustion gases between the cartridge and the combustion chamber wall. The grains cast for the Hybrid Combustion Facility tests include a blackening agent. The blackening agent, typically dye or carbon black, is necessary to ensure that radiative heat flux into the fuel grain is minimized. The fuel components are combined and heated in an 1800-W melting pot. When 110°C is reached, the melted fuel is thoroughly mixed and poured into the paper phenolic cartridge.

Depending on the grade of wax used, paraffin waxes can shrink in the range of 15–25% during solidification. To ensure that the solid fuel grain is void free, centrifugal casting is employed. Centrifugal casting will also produce a grain that is well bonded to the casing with a single circular port of the desired diameter. Two O-ring sealed end plates are fitted to the tube allowing it to be mounted on a 2-hp centrifuge. The centrifuge spins the tube about its axis at high speed (~1500 rpm) until the fuel has solidified after several hours. Once solidified, the fuel grain is removed from the centrifuge and inspected for defects. If a smaller port is required than can be achieved in a single pour, additional fuel is poured into the port, and the process is repeated. Based on visual examination, density measurements and the consistency of the regression rates for multiple-layer and single-layered grains, it has been determined that the multiple-layering technique does not produce significant radial nonhomogeneity.

This casting process consistently produces well-bonded, single-port fuel grains. The port surface is typically smooth, with less than

0.64-mm axial variation in diameter. About 1 out of every 25 grains will exhibit some minor cracking, believed to be caused by thermal stresses that arise during the solidification process. Although no grain has been cracked beyond usability, current efforts aim to explore the added benefits of annealing the fuel after casting to reduce internal stresses that develop during the solidification process. Finally, in contrast to a polymeric fuel, the residual paraffin-based fuel can be remelted and included in a new casting, thus eliminating waste.

Test Results

To date, approximately 200 tests have been carried out in the 6.1 cm (2.38 in.), that is, grain outside diameter, facility at Stanford University[6] and 41 tests (of which 29 are reported herein) in the 19.1 cm (7.5 in.), that is, grain outside diameter, facility at NASA Ames Research Center on the paraffin-based SP-1a fuel formulation. For all of the tests described here, the oxidizer was gaseous oxygen. Results from a typical test are shown in Fig. 2. Shown are the time histories for a nominal 68-atm (1000-psi) chamber pressure, 4-kg/s oxidizer mass flow rate case (test 4P-03). The supply pressure is measured upstream of the sonic orifice. The oxidizer flow is initiated at approximately $t = 0$ s and ignition takes place at $t = 1.55$ s. At $t = 9.80$ s, the oxidizer shutoff valves are closed. As can be seen in the traces, thrust termination takes a few seconds because of the large volume of oxidizer in the lines between the shutoff valves and the combustion chamber.

Out of the 29 motor tests with 28 paraffin-based fuel grains, 23 were used in data reduction to characterize the regression rate behavior of the paraffin based fuel formulation SP-1a, that is, melting temperature of 69°C. The remaining six tests were not used for the regression rate evaluation purposes for the following reasons.

1) Because of a software problem only a second after ignition, test 4F-02a-1 was shut down prematurely.

2) Test 4F-02a-2 used the same grain as test 4F-02a-1. The goal of that test was to show the reignition capability. Because the prefiring conditions of the grain were not known, that successful run could not be used to evaluate the regression rate and the average oxidizer mass flux in the port.

3) During run 4F-03, the stainless steel injector (used to replace a brass injector) ignited and started a metal fire at the fore end of the motor. We have decided against using the data from this run, due the unknown influence of the excess metallic mass generated at the fore-end on the regression rate characteristics of the fuel. Following this test, a replacement injector made of copper was installed, and this has been used successfully ever since.

4) Tests 4L-06 and 4L-07, which were conducted with small port diameters, that is, ~7.62 cm (3.00 in.) corresponding to 84% vol-

umetric loading, resulted in excessive fuel regression rates. After visual examination of the grains after firing, we have concluded that the excessive fuel mass generation observed in these tests is a result of the structural failure, that is, possible crack formation, of the port internal surface. It can be shown that, for small port diameter to grain outside diameter ratios, the chamber pressure loading can generate high tensile hoop stresses on the inner surface of the fuel grain. This fuel structural disintegration theory is supported by the relatively low efficiencies estimated for these tests. Further investigation is needed to develop a more conclusive explanation of this phenomenon.

5) During test 4L-11, the control system prematurely terminated the GOX flow. The burn time for this run is not adequate for accurate data reduction.

Data Analysis

In the following sections, the results obtained from the reduced test data will be discussed. The data reduction techniques are discussed in Appendices A and B, and a summary of the test results is given in Tables 1 and 2. We concentrate on four key areas: 1) regression rate law determination, 2) motor efficiency evaluation, 3) ignition characteristics, and 4) motor stability evaluation.

Regression Rate

Regression rate is the most important characteristic of a hybrid rocket fuel, and a complete characterization of that quantity as a function of all the relevant operational variables of the hybrid motor is critical for the satisfactory design of a practical system.

Effect of Oxidizer Mass Flux

The averaged regression rates as a function of the averaged oxidizer mass fluxes for all of the tests accepted for data reduction are shown in Fig. 3. A curve fit to the data points, that is, both laboratory-scale and larger scale, results in a mass flux exponent of 0.62 [subsequent Eq. (2)]. Note that this value is slightly smaller than the flux exponents commonly observed in classical propellants. Note that a low mass flux exponent is desirable because this would reduce the extent of the O/F shift during the course of the motor operation and improve the I_{sp} efficiency of the propulsion system. The regression rate law[9] for the classical fuel HTPB (burned with liquid oxygen) has also been plotted in Fig. 3 for comparison purposes.

Effect of Chamber Pressure

Several tests at pressures ranging from 21.6 to 67.6 atm were conducted around an intermediate mass flux level of 27.5 g/cm² · s
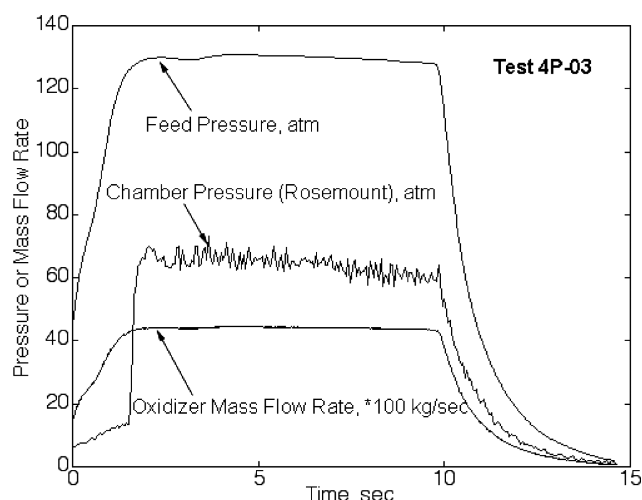

Fig. 2   Time histories of chamber pressure and oxygen mass flow rate from a typical run.
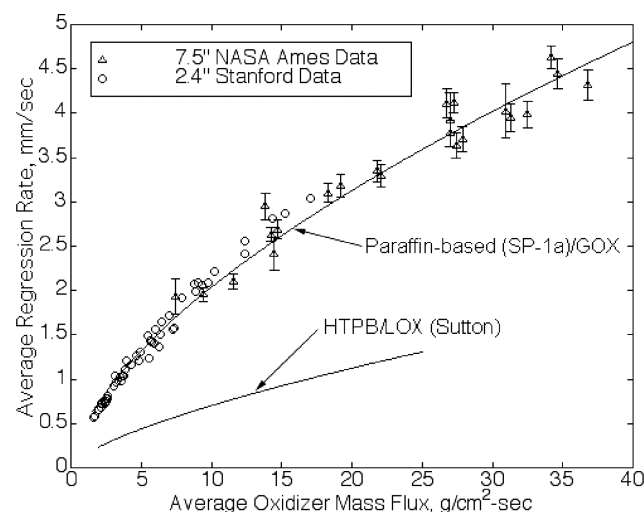

Fig. 3   Regression rate data for the paraffin-based fuel SP-1a.

Table 1 Motor test conditions and notes

Test[a]	Orifice diameter, mm	Initial port diameter, m	Grain length, m	Initial nozzle throat diameter, mm	Actual burn time, s	Notes
ST	14.2	0.101	0.775	50.3	7.00	Cracked fuel grain
4F-2	11.4	0.092	0.775	36.8	9.25	Nozzle failure
4F-1	11.4	0.112	0.775	37.1	9.35	Successful test
4F-2a-1	Premature shutdown, software failure. No data reduction.					
4F-2a-2	Fuel grain of 4F2a-1 is refired. No data reduction.					
4F-1a	14.2	0.130	0.775	50.3	7.60	Nozzle erosion/good test
4F-4	14.2	0.100	0.775	50.3	8.50	Nozzle erosion/good test
4F-5	14.2	0.091	0.775	50.3	8.20	Nozzle erosion/good test
4F-3	Injector fire. No data reduction.					
4F-1b	11.4	0.112	0.775	36.8	9.50	Successful test
4Thr-1	11.4	0.089	0.775	36.8	10.50	Successful test/throttling
4F-1c	11.4	0.130	0.775	36.8	10.35	Successful test
4F-3a	14.2	0.113	0.775	50.3	8.30	Successful test
4L-01	14.2	0.113	1.148	50.3	8.45	Successful test
4P-01	14.2	0.114	1.148	71.1	8.40	Successful test
4P-02	14.2	0.117	1.148	41.1	7.25	Successful test
4P-03	14.2	0.112	1.148	41.1	8.25	Successful test
4L-03	14.2	0.141	1.148	50.3	6.20	Successful test
4L-04	14.2	0.089	1.148	50.3	8.30	Successful test
4L-05	14.2	0.100	1.148	50.3	8.25	Successful test
4L-06	14.2	0.076	1.148	50.3	8.20	Fuel port failure
4L-07	14.2	0.075	1.148	51.8	8.00	Fuel port failure
4L-08	14.2	0.103	1.148	56.2	8.15	Successful test
4I-01	14.2	0.113	1.148	71.3	8.25	Successful test
4P-04	11.4	0.113	1.148	71.6	8.15	Successful test
4L-09	14.2	0.090	1.148	55.6	8.15	Successful test
4L-10	17.3	0.113	1.148	61.3	8.20	Successful test
4L-11	14.2	0.154	1.148	51.3	2.55	Control system failure
4L-12	11.4	0.103	1.148	51.3	7.30	Successful test

[a]I, ignition test, L, length variation test, and P, pressure variation test.

Table 2 Motor test results

Test	Oxidizer mass flow rate, kg/s	Initial oxidizer flux, g/cm²·s	Average oxidizer flux, g/cm²·s	Regression rate, mm/s	O/F	Chamber pressure, atm	C* efficiency
ST	2.07	27.12	16.66	3.59	2.18	20.9	0.78
4F-2	2.06	31.65	18.33	3.09	2.67	11.1	——
4F-1	2.03	20.87	14.47	2.40	3.05	35.9	0.85
4F-2a-1	Premature shutdown-software failure. No data reduction.						
4F-2a-2	Fuel grain of 4F2a-1 is refired. No data reduction.						
4F-1a	4.02	——	21.75	3.37	3.89	34.1	0.91
4F-4	4.24	——	30.92	4.04	3.97	35.9	0.90
4F-5	4.32	64.32	33.89	4.69	3.54	37.5	0.88
4F-3	Injector fire. No data reduction.						
4F-1b	2.13	21.58	14.22	2.65	2.72	38.2	0.85
4Thr-1	1.56	35.00	13.76	2.97	2.02	28.4	0.77
4F-1c	2.07	15.88	11.45	2.15	3.00	36.9	0.89
4F-3a	4.39	44.89	27.13	3.90	3.84	38.6	0.90
4L-01	4.40	44.49	27.05	3.66	2.57	45.7	0.88
4P-01	4.43	44.36	27.41	3.52	2.69	21.6	0.82
4P-02	4.42	39.23	26.96	3.82	2.48	67.6	0.87
4P-03	4.41	43.31	27.88	3.58	2.65	63.9	0.88
4L-03	4.45	29.11	22.05	3.18	2.69	43.7	0.84
4L-04	4.44	72.46	36.80	4.17	2.66	44.7	0.85
4L-05	4.43	57.57	32.44	3.84	2.72	44.1	0.85
4L-06	4.40	98.80	36.87	5.72	1.97	46.2	0.80
4L-07	4.43	102.73	33.77	6.73	1.63	44.4	0.80
4L-08	4.42	54.32	31.29	3.82	2.64	35.7	0.85
4I-01	4.47	43.62	26.76	4.02	2.40	21.7	0.78
4P-04	2.11	22.79	14.69	2.74	1.78	10.8	0.78
4L-09	2.05	32.85	19.21	3.26	1.70	18.0	0.80
4L-10	5.55	55.25	34.66	4.25	2.89	40.1	0.88
4L-11	1.47	8.68	7.43	2.00	1.56	14.4	0.78
4L-12	2.08	11.06	9.40	1.96	2.01	20.5	0.79

(Fig. 4). It has been determined that the effect of pressure on the regression rate is negligible. The lack of pressure effect must be checked at very low and very high fluxes, where the classical hybrids shows some pressure dependency.

Effect of Grain Length

A significant effect of grain length on regression rate is not observed either going from the laboratory-scale to the HCF scale, that is, factor of seven in grain length, or on going from one length to the other in the HCF testing. (See Fig. 5 for the latter result, where grains of two different length are compared.) For all of the tests, the regression rate along the axis of the grain was quite uniform. Only a small increase, that is, less than 10%, in the regression rate with increasing distance from the fore end has been observed. This coning effect has only been detected at high flux tests. Low and moderate flux tests showed axially uniform burning.
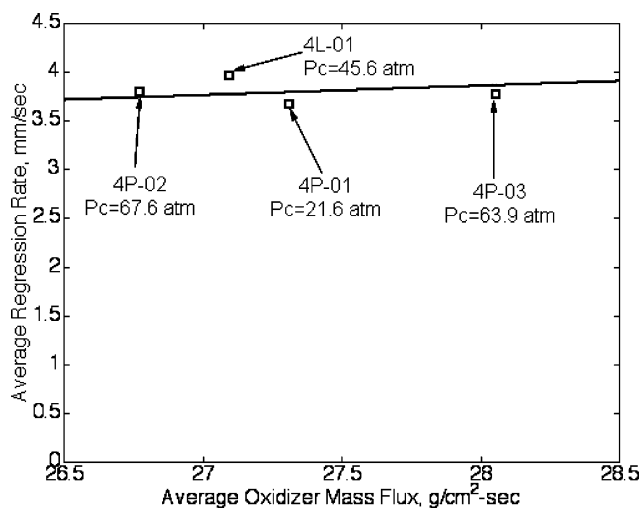
Fig. 4 Effect of chamber pressure on the regression rate behavior for paraffin-based propellant SP-1a.
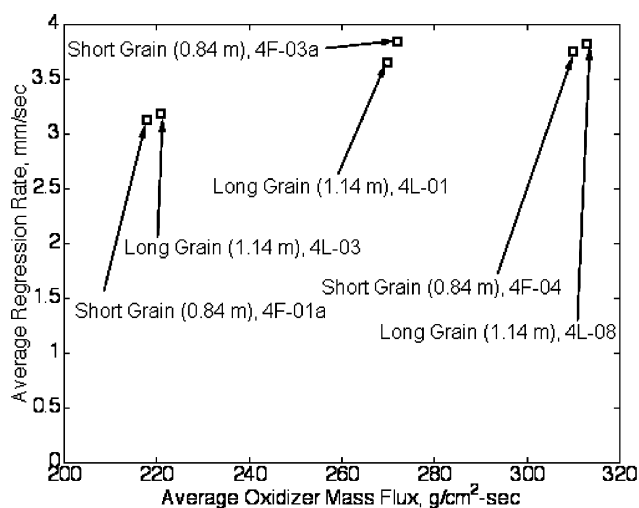

Fig. 5 Effect of fuel grain length on the regression rate behavior for paraffin-based propellant SP-1a.

Effect of O/F Ratio

A correction for the O/F ratio effect on the regression rate has been developed and applied to the laboratory-scale Stanford University data and also to the HFC data. The correction formula used in the calculations is

$$\frac{\bar{r}}{a\bar{G}_{ox}^n L_g^m} = \left(\frac{1}{1+m}\right)\left\{(1-n)\Big/\left[\left(1+\frac{1}{O/F}\right)^{1-n}-1\right]\frac{O}{F}\right\} \quad (1)$$

where a is the regression rate constant and m is the length exponent, which is determined to be zero. This formula is derived by taking the space average of the local regression rate expression, and the derivation is outlined in Appendix B. It has been observed that the correction, based on the proceeding formula, which can be as large as 5–7% in the most extreme cases, reduces the scatter in the regression rate data. Note that the data points shown in Figs. 3–5 are corrected for the O/F variation.

Based on the arguments of this section, we suggest the following regression rate law for the paraffin-based fuel, SP-1a.

$$\bar{r} = 0.488\bar{G}_{ox}^{0.62} \quad (2)$$

The regression rate is in millimeter per second and oxidizer mass flux is gram per square centimeter per second. This formula can be used with reasonable accuracy within the motor O/F ratio range of

1.7–2.3. For O/F ratios significantly out of this range, we recommend the following equation, which includes the O/F correction:

$$\bar{r} = 0.163\bar{G}_{ox}^{0.62}\Big/\left[\left(1+\frac{1}{O/F}\right)^{0.38}-1\right]\frac{O}{F} \quad (3)$$

Efficiency

Efficiencies based on c^* are used for all motor tests. The efficiency values estimated for all motor tests are listed in Table 2. (See Appendix A for the estimation method.) It has been determined that the efficiency increases with increasing motor L^* (caused by the increased residency time), increasing mass flux (caused by reduced droplet size), and increasing motor O/F (possibly related to increased exposure of the droplets to the oxidizer). Note that L^* is defined as the ratio of the average combustion chamber volume to the average nozzle throat area. The delivered c^* values calculated from data are plotted against motor O/F data in Fig. 6. It can be seen from Fig. 6 that the motor efficiencies improve with increasing O/F ratio, and at an O/F ratio of 2.7, for which the theoretical I_{sp} is also maximized for the SP-1a propellant system, the motor efficiency range is 85–90%. Figure 7 shows the efficiency as a function of the motor L^* for the motors running in the same O/F and mass flux range. It is clear that the efficiency improves with increasing L^*, indicating the encouraging result that larger-scale systems would run at higher efficiencies. Note that efforts specifically directed at improving the efficiency have not been attempted to date in this program.
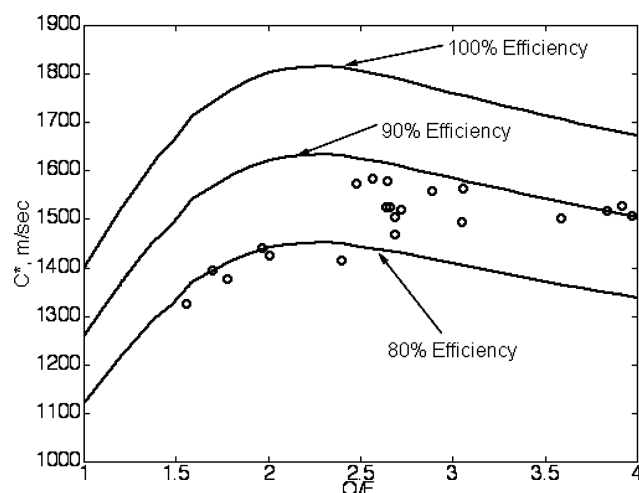

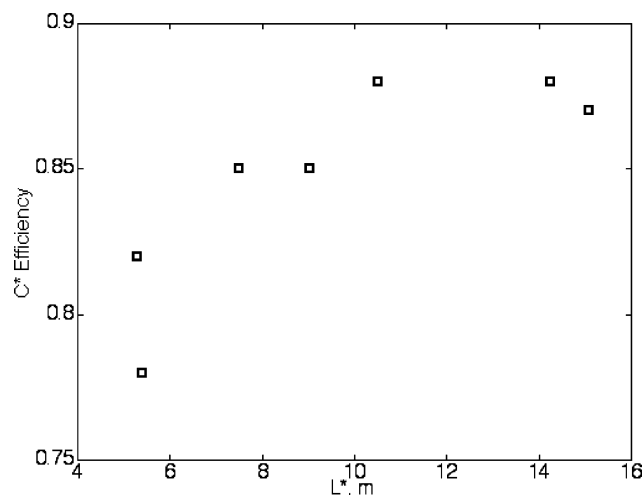**Fig. 6 Motor delivered c^* as a function of O/F.**

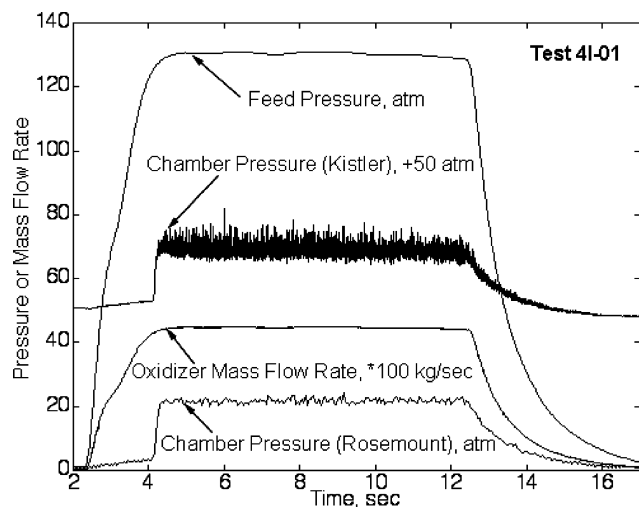**Fig. 7 Motor c^* efficiency as a function of motor L^*.**

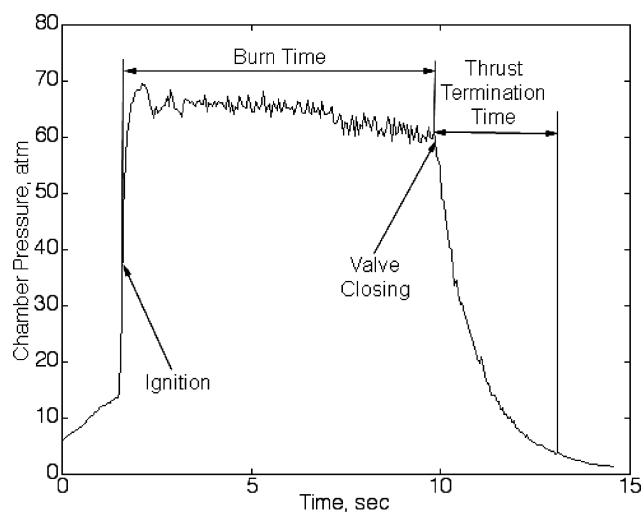Fig. 8 Data acquired during operation for test 4P-01.

Fig. 9 Chamber pressure–time trace for the run 4P-03.

Ignition

The methane/GOX ignition system is successfully tuned to achieve smooth reliable ignition for all of the test conditions. Figures 2, 8, and 9 show the short-ignition transient times and the small-ignition overshoots typically achieved in our tests. The pressure time traces of all of the motors generally showed the characteristics of classical hybrid rockets, a slight down slope with time due to the opening of the fuel port and nozzle throat. Toward the end of the run, nozzle erosion accelerates the time decay of chamber pressure slightly as can be seen in Figs. 2, 8, and 9.

Combustion Stability

The facility is equipped with a fast response Kistler pressure transducer to permit spectral analysis of the pressure time history. Figure 10 shows data from one of the 20.4-atm (300-psi) chamber pressure runs. The rms of the pressure oscillations considered over 1-s time intervals varied between 4 and 12% of the mean pressure. The amplitude spectrum of the pressure fluctuations typically contained three distinct peaks at around 30, 100, and 350 Hz. The most dominant of these peaks is that at around 30 Hz, which is believed to be caused by a coupling between the delay in the boundary layer responding to any changes in mass flow and the thermal lag in the solid fuel. The mechanism of this instability is described by Karabeyoglu and Altman,[10] and Karabeyoglu et al.[11] The peaks at around 100 and 350 Hz were associated with the bulk mode and the acoustic half-wave in the combustion chamber, respectively. A more detailed description of these combustion oscillations is presented in Ref. 12.
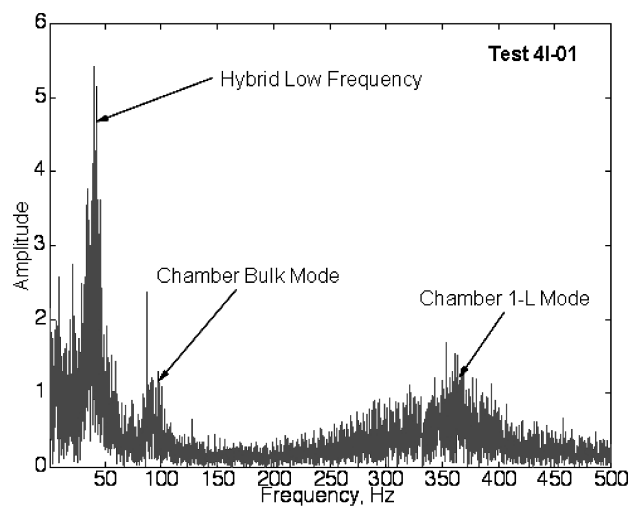

Fig. 10 Pressure spectrum for test 4P-01.

Grain Structural Integrity

The paraffin-based grains used in the tests showed good structural integrity even at high chamber pressures (68 atm). A structural failure has observed only twice with grains with very small port diameters that were subject to large tensile bore stresses. (Note that these failures were benign.) The excessive heating and melting of the fuel inside the grain during motor firings was not evident. This is possibly due to the low heat conductivity of paraffin and the radiation absorber used in the formulation.

Although a detailed structural evaluation of paraffin-based fuels is beyond the scope of this paper, we note that a preliminary evaluation of the strength and viscoelastic properties of paraffin-based fuel, SP-1a, indicated good structural integrity under typical loading conditions. A detailed treatment of viscoelastic behavior of paraffinic fuels is given in Ref. 13.

Conclusions

The fast burning nontoxic and nonhazardous fuel SP-1a clearly presents a significant improvement over conventional polymeric fuels. The regression rates measured for paraffin-based fuel SP-1a, at two different scales, that is, the 6.1 cm (2.38-in.)-diam Stanford University motor and the 19.1 cm (7.5-in.)-diam HCF motor, are approximately three times larger than the regression rates of the classical hybrid fuel HTPB. The highest average and initial oxidizer fluxes tested so far in the program are 36.9 and 102.7 g/cm$^2 \cdot$ s, respectively. These values are well into the range of fluxes that would be used in an operational hybrid propulsion system. The highest chamber pressure tested so far is close to 68 atm (1000 psi). The mechanism (postulated to be droplet entrainment from an unstable liquid layer on the surface of the fuel) leading to the high regression rate seems to be still active at those large fluxes and chamber pressures and for grains that are seven times longer than the Stanford University motor. No length or pressure dependency on the regression rate is observed.

The efficiencies of the motors tested range between 80 and 90%. It appears that motors that are operated at higher fluxes tend to generate higher efficiencies. This observation is consistent with the theoretical understanding of the entrainment process because at higher flux levels the droplet sizes that are entrained into the gas stream are predicted to be smaller. Efficiency also increases with increasing L^* and motor O/F.

The test results, the pressure time history, and the regression rate behavior are highly reproducible. In summary, the main conclusions from these scale-up tests are as follows.

1) The high regression rate behavior observed in the small-scale tests at Stanford University prevails when the motor is scaled up to chamber pressures and mass fluxes characteristic of operational systems. Moreover, the regression rate data from large and small motors match quite well, indicating that small-scale tests can be used to infer behavior of larger motors. This is extremely useful

when it comes to developing the right fuel formulation for a given mission.

2) No length or pressure effect is observed on the regression rate. The regression rate along the axis of the grain has been observed to be uniform.

3) Paraffin-based fuels provide reliable ignition and stable combustion over the entire range of mass fluxes encountered (2–102 $g/cm^2 \cdot s$).

4) The fuel exhibited good structural integrity over the range of chamber pressures used, 10–68 atm (150–1000 psi).

Appendix A: Data Reduction Details

Regression Rate

The space–time averaged regression rate for a given test is estimated from initial port diameter and consumed fuel mass measurements. The following relations are used in the calculations:

$$\bar{\dot{r}} = \frac{d_{vc} - d_i}{2t_b} \qquad (A1a)$$

$$d_f = \left[d_i^2 + \frac{4\Delta M_f}{\pi \rho_f L_g} \right]^{\frac{1}{2}} \qquad (A1b)$$

Here d_{vc} is the port diameter at the start of the thrust termination event, ΔM_f is the total mass of the fuel burned, that is, difference of two weight measurements before and after the test, and L_g is the fuel grain length. The fuel density ρ_f is taken to be 0.92 $g/cm^2 \cdot s$ based on independent density measurements. The burn time t_b is defined as the time between the ignition and the valve closing events shown in Fig. 9 for the motor test 4P-03. As evident from Fig. 9, the thrust termination response of the feed system is slow due to the large volume of oxygen feed system piping. Because a significant amount of fuel is consumed during the thrust termination process, the regression rate measurement must be corrected for an accurate characterization of the regression rate behavior. We have developed a correction procedure based on an estimation of the port diameter change during thrust termination transient. For an exponential oxidizer mass flow rate decay function, the relation between the final port diameter and the port diameter at the start of the thrust termination event is determined to be

$$d_{vc} = \left(\left\{ [(2n+1)/n](2^{n+1}/\pi^n)\tau_{fs}a\dot{m}_{ox}^{ter}[1 - \exp(-nt_f/\tau_{fs})] \right\} + d_f^{2n+1} \right)^{1/(2n+1)} \qquad (A2)$$

The differential equation relating the port diameter change to the regression rate expression ($\dot{r} = a\,G_{ox}^n$) is integrated to obtain Eq. (A2). Note that a and n are the regression rate coefficient and exponent for the propellant system of interest and $\dot{m}_{ox}^{ter}$ is the oxidizer mass flow rate at the start of the thrust termination event. In Eq. (A2), the characteristic timescale of the feed system is defined as

$$\tau_{fs} = V_f \big/ A_{or} c_{ox}^* \Gamma^2 \qquad (A3)$$

where

$$\Gamma = \sqrt{\gamma}[2/(\gamma+1)]^{(\gamma+1)/2(\gamma-1)}$$

Here V_f is the volume of the feed system piping (estimated to be 0.017 m^3), A_{or} is the oxidizer feed system orifice area, and c_{ox}^* is the characteristic velocity for the oxygen gas at ambient temperature. For the data reduction, the characteristic emptying time of the feed system is estimated from the pressure time data by fitting an exponential function. Thus, the error that would be introduced by using Eq. (A3) is eliminated. For certain testing conditions, this characteristic time can be as long as 1.5 s, a significant period compared to the nominal burn time of 8 s. The time variable t_f is defined as the time after the main valve closing event that the fuel regression rate becomes negligible. For all calculations, we have used a t_f/τ_{fc} ratio of 1.0. It has been determined that the effect of the t_f/τ_{fc} ratio on the regression rate correction diminishes significantly for values

larger than 1.0 due to the exponential nature of the oxidizer mass flow rate decay.

Also note that, unlike the thrust termination transient, the ignition event is fast compared to the overall burn time, making an ignition correction unnecessary.

Oxidizer Mass Flow Rate

The oxidizer mass flow rate is measured by two means: 1) sonic orifice and 2) calibrated venturi, both inserted in the main oxidizer line. For the sonic orifice measurement, with the choked flow assumption (which is valid for the whole duration of the test), the mass flow rate can be expressed as

$$\dot{m}_{ox} = P_f A_{or} C_D \big/ c_{ox}^* \qquad (A4)$$

The discharge coefficient C_D for the thick square edge orifice is taken as 0.84 as recommended in Ref. 14. The mass flow calculations for the venturi are based on the equations suggested in Ref. 15. The two mass flow rate measurement methods are determined to be in good agreement for all of the tests, that is, typically the difference is less than 1%. The only deviation is observed during transients, for which the venturi measurement becomes questionable (because the quasi-steady assumption is violated). The average oxidizer mass flow rate $\bar{\dot{m}}_{ox}$ is estimated over the course of the burn, from the ignition event to the valve closing event.

Oxidizer Mass Flux

It is suggested in the literature[1] that the local instantaneous regression rate of a hybrid fuel depend on the local instantaneous mass flux because this is what can be accurately measured. However, it is much more convenient to present the regression rate law of a propellant system in terms of the space–time averaged regression rate vs the space–time averaged mass flux. Even though the space–time averaged regression rate is a well-defined quantity, the selection of a particular mass flux averaging method is necessary. For the purposes of this paper, we use the oxidizer mass flux based on the averaged port diameter over the course of the run,

$$\bar{G}_{ox} = \frac{16\bar{\dot{m}}_{ox}}{\pi(d_i + d_{vc})^2} \qquad (A5)$$

It can be shown that the average diameter method, that is, as opposed to the average area or average flux methods, results in the most accurate representation of the hybrid regression rate law. The selection of the oxidizer mass flux G_{ox} rate over the total mass flux G_{tot} is completely arbitrary because both cases should be corrected for the average O/F ratio of the motor. The correction formula for the oxidizer mass flux case is given in Eq. (1).

Combustion Efficiency

The combustion efficiency, that is, c^* efficiency, of the motor is calculated based on the following equation:

$$\eta_c = c_{act}^* \big/ c_{theo}^* \qquad (A6)$$

The measured characteristic velocity c_{act}^* for each test is estimated with use of the following relation:

$$c_{act}^* = \frac{\int_0^{t_b + t_f} P_c \, dt}{(\Delta M_{ox} + \Delta M_f)C_d \bar{A}_n} \qquad (A7)$$

Note that the pressure integral includes the regular test period and the thrust termination event. Here $\bar{A}_n$ is the average nozzle area, C_d is the nozzle discharge coefficient, and ΔM_{ox} is the total oxidizer mass consumed during the regular test and the thrust termination periods. The theoretical characteristic velocity c_{theo}^* is evaluated at the average motor O/F $= \Delta M_{ox}/\Delta M_f$. The nozzle discharge coefficient is taken as 0.99 for all tests.

We finally note that, for most of motor tests reported in this paper, the total igniter gas mass is less than 30 g. Thus, the effect of the igniter mass on the regression rate and efficiency measurements is negligible.

Error Analysis

An error analysis has been conducted to quantify the uncertainties in the reduced variables such as the regression rate and the oxidizer mass flux. For the purposes of this analysis, it is convenient to rearrange Eq. (A2) in the following nondimensional form:

$$D_{\text{ratio}} \equiv d_{\text{vc}}/d_f = \{1 - [2(2n+1)/n]Re^{-T}\}^{1/(2n+1)} \quad \text{(A8)}$$

Here the following nondimensional variables are introduced:

$$R = \tau_{\text{fs}}\dot{r}^{\text{ter}}\big/d_f, \qquad T = nt_f/\tau_{\text{fs}}$$

Note that $\dot{r}^{\text{ter}}$ is the fuel regression rate at the start of the thrust termination event. Because $\dot{r}^{\text{ter}}$ is not readily known, it is convenient to use the following approximate formula to evaluate the value of R:

$$R \cong 0.25(\tau_{\text{fs}}/t_b)(1 + d_i/d_f)^2(1 - d_i/d_f) \quad \text{(A9)}$$

Based on Eq. (A8), the relative error in estimating the port diameter at thrust termination, E_{dvc}, can be expressed in terms of the relative errors in d_f, R, and T (see Ref. 16),

$$E_{dvc} = \left[E_{df}^2 + (f_R E_R)^2 + (f_T E_T)^2\right]^{\frac{1}{2}} \quad \text{(A10)}$$

Note that the relative error is defined as the ratio of the absolute error to the mean value of the quantity. Here the sensitivity parameters can be calculated by using the following expressions:

$$f_R = 2R(1 - e^{-T})/n, \qquad f_T = f_R[Te^{-T}/(1 - e^{-T})]$$

The relative error in the final diameter, E_{df}, can be written in terms of the relative measurement errors in fuel grain mass loss, $E_{\Delta M}$, fuel density, E_{ρ}, and grain length, E_L with use of Eq. (A1b).

$$E_{df} = 0.5(1 + d_i/d_f)\left[E_{\Delta M}^2 + E_{\rho}^2 + E_L^2\right]^{\frac{1}{2}} \quad \text{(A11)}$$

Similarly, the relative error in the regression rate estimation, E_r, can be written in terms of the relative errors in the port diameter at thrust termination, E_{dvc}, initial port diameter, E_{di}, and the burn time, E_t,

$$E_r = \left[\left(\frac{d_{\text{vc}}/d_i}{d_{\text{vc}}/d_i - 1}E_{dvc}\right)^2 + \left(\frac{1}{d_{\text{vc}}/d_i - 1}E_{di}\right)^2 + E_t^2\right]^{\frac{1}{2}} \quad \text{(A12)}$$

By the use of Eqs. (A8–A11), the error in regression rate can be estimated based on the measurement errors in initial port diameter, fuel weight reduction, fuel density, grain length, and burn time. Note that the relative error in the regression rate decreases with increasing diameter ratio, d_{vc}/d_i, or web thickness burned. For a typical test with the following parameters and measurement errors, the relative and absolute errors in regression rate can be estimated to be 0.051 and 0.159 mm/s, respectively: $\bar{r} = 3.130$ mm/s, $n = 0.62$, $t_b = 8.00$ s, $t_f = 1.50$ s, $\tau_{\text{fs}} = 1.50$ s, $d_i = 10.16$ cm, $d_f = 15.66$ cm, $E_R = 0.010$, $E_T = 0.200$, $E_{\Delta M} = 0.010$, $E_{\rho} = 0.011$, $E_L = 0.002$, $E_{di} = 0.008$, and $E_t = 0.013$.

Similarly, Eqs. (A4) and (A5) can be used to determine the relative error in the oxidizer mass flux, E_{Gox},

$$E_{\text{Gox}} = \left[\left(2\frac{d_{vc}/d_i}{d_{vc}/d_i + 1}E_{dvc}\right)^2 + \left(\frac{2}{d_{vc}/d_i + 1}E_{di}\right)^2 + E_{mox}^2\right]^{\frac{1}{2}} \quad \text{(A13)}$$

Based on the orifice equation, the relative error in the oxidizer mass flow rate, E_{mox}, can be calculated in terms of the relative errors in the average feed pressure, E_{Pf}, orifice diameter, E_{do}, orifice discharge coefficient, E_{Cd}, and ambient temperature, E_{To},

$$E_{mox} = \left[E_{Pf}^2 + (2E_{do})^2 + E_{Cd}^2 + (E_{To}/2)^2\right]^{\frac{1}{2}} \quad \text{(A14)}$$

For a typical test characterized by the following the conditions, the relative and absolute errors associated with the oxidizer mass flux estimation can be calculated to be 0.037 and 0.730 g/cm$^2 \cdot$ s,

respectively: $\bar{G}_{\text{ox}} = 20.0$ g/cm$^3 \cdot$ s, $E_{Pf} = 0.020$, $E_{do} = 0.001$, $E_{Cd} = 0.024$, and $E_{To} = 0.010$.

Figure 3 shows the regression rate error bars estimated for the HFC motor tests reported in this paper. Note that some of the tests have error estimates significantly larger than the nominal values. All of these cases showed some kind of an anomalous behavior (such as burning on the outside surface of the fuel grain) that has compromised the accuracy of the regression rate estimate.

Similar analysis has been performed on the Stanford University motor data and an absolute error of 0.163 mm/s has been established for typical test conditions. The regression rate error bars for the Stanford University data are not included in Fig. 3 for the sake of clarity.

Appendix B: Derivation of the Space-Averaged Regression Rate Formula

According to the diffusion limited theory developed by Marxman et al.,[1] the local instantaneous regression speed of the hybrid fuel can be expressed as a power law formula in terms of the local mass flux and the axial location in the port,

$$\dot{r} = aG^n x^m \quad \text{(B1)}$$

The coefficient a can be assumed to be constant for a given combination of propellants. Note that under extreme mass flux conditions, that is, very high or very low, the regression rate expression for a hybrid becomes pressure dependent. In this case, the coefficient a can be written as a function of the chamber pressure. For the operating conditions encountered in typical hybrid rocket applications, the effect of pressure on the regression rate is negligible, and for the sake of simplicity it will be ignored in the following derivation.

The mass balance in the port can be expressed as

$$\frac{d\dot{m}}{dx} = \rho_f C_{\text{port}}\dot{r} \quad \text{(B2)}$$

where C_{port} is the circumference of the port. The mass flow rate derivative can be written in terms of local mass flux G and port area A_{port},

$$\frac{d\dot{m}}{dx} = \frac{dG A_{\text{port}}}{dx} = A_{\text{port}}\frac{dG}{dx} + G\frac{dA_{\text{port}}}{dx} \quad \text{(B3)}$$

For typical hybrid applications, the change in the port area is small compared to the change in the mass flux, that is,

$$A_{\text{port}}\frac{dG}{dx} \gg G\frac{dA_{\text{port}}}{dx} \quad \text{(B4)}$$

Thus, Eq. (B3) can be simplified to

$$A_{\text{port}}\frac{dG}{dx} = a\rho_f C_{\text{port}}G^n x^m \quad \text{(B5)}$$

After the introduction of the dimensional parameter B_G, Eq. (B5) becomes

$$\frac{dG}{G^n} = B_G x^m dx \quad \text{(B6)}$$

Integration of this total differential yields the following mass flux distribution in the port,

$$G/G_{\text{ox}} = \left[1 + \alpha(x/L_g)^{(m+1)}\right]^{1/(1-n)} \quad \text{(B7)}$$

where

$$\alpha = [(1-n)/(1+m)]B_G\left(L_g^{m+1}\big/G_{\text{ox}}^{n-1}\right)$$

On substitution of Eq. (B7) into Eq. (B1), the local instantaneous regression rate can be written explicitly as

$$\dot{r} = aG_{\text{ox}}^n L_g^m\left[1 + \alpha(x/L_g)^{(m+1)}\right]^{n/(1-n)}(x/L_g)^m \quad \text{(B8)}$$

The space averaged regression rate can be defined as

$$\bar{\dot{r}} = \int_0^1 \dot{r}(x/L_g)\,\mathrm{d}(x/L_g) \tag{B9}$$

This equation can be integrated by parts to yield the following closed-form solution:

$$\bar{\dot{r}} = \frac{aG_{\mathrm{ox}}^n L_g^m (1-n)}{\alpha(1+m)} \left[(1+\alpha)^{1/(1-n)} - 1\right] \tag{B10}$$

Independently, average regression rate and O/F ratio of the motor are related according to the expression

$$\bar{\dot{r}} \big/ aG_{\mathrm{ox}}^n L_g^m = [1/(\mathrm{O/F})](1/B_G)\left(G_{\mathrm{ox}}^{1-n} \big/ L_g^{1-m}\right) \tag{B11}$$

where the O/F ratio is

$$\frac{\mathrm{O}}{\mathrm{F}} = \frac{G_{\mathrm{ox}} A_{\mathrm{port}}}{\rho_f L_g C_{\mathrm{port}} \bar{\dot{r}}} \tag{B12}$$

Also from the definition of α,

$$\bar{\dot{r}} \big/ aG_{\mathrm{ox}}^n L_g^m = [1/(\mathrm{O/F})][(1-n)/(1+m)](1/\alpha) \tag{B13}$$

After combining Eqs. (B11) and (B13), one obtains the following formula for α:

$$\alpha = [1 + 1/(\mathrm{O/F})]^{1-n} - 1 \tag{B14}$$

On substitution of this expression for α in Eq. (B13), one finds the exact expression for the space averaged regression rate,

$$\frac{\bar{\dot{r}}}{aG_{\mathrm{ox}}^n L_g^m} = \frac{1}{1+m}\left\{ (1-n) \bigg/ \left[\left(1 + \frac{1}{\mathrm{O/F}}\right)^{1-n} - 1\right]\frac{\mathrm{O}}{\mathrm{F}}\right\} \tag{B15}$$

Acknowledgments

References

[1] Marxman, G. A., Wooldridge, C. E., and Muzzy, R. J., *Fundamentals of Hybrid Boundary Layer Combustion*, Progress in Astronautics and Aeronautics, Vol. 15, AIAA, New York, 1964, pp. 485–522.

[2] Altman, D., "Hybrid Rocket Propulsion, Prospects for the Future," *Proceedings of the AIAA 50th Anniversary Meeting*, May 1981.

[3] Calabro, M., "European Hybrid Propulsion History," *Proceedings of the 29th Aerospace Sciences Meeting*, 10 May 1991.

[4] Altman, D., "Hybrid Rocket Development History," AIAA Paper 91-2515, June 1991.

[5] Karabeyoglu, M. A., "Transient Combustion in Hybrid Rockets," Ph.D. Dissertation, Dept. of Aeronautics and Astronautics, Stanford Univ., Stanford, CA, Aug. 1998.

[6] Karabeyoglu, M. A., Cantwell, B. J., and Altman, D., "Development and Testing of Paraffin-Based Hybrid Rocket Fuels," AIAA Paper 2001-4503, July 2001.

[7] Karabeyoglu, M. A., Altman, D., and Cantwell, B. J., "Combustion of Liquefying Hybrid Propellants, Part 1: General Theory," *Journal of Propulsion and Power*, Vol. 18, No. 3, 2002, pp. 610–620.

[8] Karabeyoglu, M. A., and Cantwell, B. J., "Combustion of Liquefying Hybrid Propellants, Part 2: Stability of Liquid Films," *Journal of Propulsion and Power*, Vol. 18, No. 3, 2002, pp. 621–630.

[9] Sutton, G., *Rocket Propulsion Elements*, 6 ed., Wiley-Interscience, New York, 1992, pp. 512–513.

[10] Karabeyoglu, M. A., and Altman, D., "Dynamic Modeling of Hybrid Rocket Combustion," *Journal of Propulsion and Power*, Vol. 15, No. 4, 1999, pp. 562–571.

[11] Karabeyoglu, M. A., De Zilwa, S., Cantwell, B. J., and Zilliac, G., "Transient Modeling of Hybrid Rocket Low Frequency Instabilities," AIAA Paper 2003-4463, July 2003.

[12] De Zilwa, S., Zilliac, G., Karabeyoglu, A., and Reinath, M., "Combustion Oscillations in High Regression Rate Hybrid Rockets," AIAA Paper 2003-4465, July 2003.

[13] Kilic, S., Karabeyoglu, M. A., Stevens, J., and Cantwell, B. J., "Modeling the Slump Characteristics of the Hydrocarbon-Based Hybrid Rocket Fuels," AIAA Paper 2003-4461, July 2003.

[14] Ward-Smith, A. J., "Critical Flowmetering: The Characteristics of Cylindrical Nozzles with Sharp Upstream Edges," *International Journal of Heat and Fluid Flow*, Vol. 1 No. 3, 1979, pp. 123–132.

[15] Miller, W. R., *Flow Measurement Engineering Handbook*, 3rd ed., McGraw-Hill, New York, 1996, Chap. 10.

[16] Bevington, P. R., *Data Reduction and Error Analysis for the Physical Sciences*, McGraw–Hill, New York, 1969, Chap. 4.